

A Three-Level Whole-Body Disturbance Rejection Control Framework for Dynamic Motions in Legged Robots

Bolin Li, Gewei Zuo, Zhixiang Wang, Xiaotian Ke, Lijun Zhu, and Han Ding

Abstract—This paper presents a control framework designed to enhance the stability and robustness of legged robots in the presence of uncertainties, including model uncertainties, external disturbances, and faults. The framework enables the full-state feedback estimator to estimate and compensate for uncertainties in whole-body dynamics of the legged robots. First, we propose a novel moving horizon extended state observer (MH-ESO) to estimate uncertainties and mitigate noise in legged systems, which can be integrated into the framework for disturbance compensation. Second, we introduce a three-level whole-body disturbance rejection control framework (T-WB-DRC). Unlike the previous two-level approach, this three-level framework considers both the plan based on whole-body dynamics without uncertainties and the plan based on dynamics with uncertainties, significantly improving payload transportation, external disturbance rejection, and fault tolerance. Third, simulations of both humanoid and quadruped robots in the Gazebo simulator demonstrate the effectiveness and versatility of T-WB-DRC. Finally, extensive experimental trials on a quadruped robot validate the robustness and stability of the system when using T-WB-DRC under various disturbance conditions.

I. INTRODUCTION

Legged robots have attracted considerable attention in recent years due to their capability to traverse complex and uneven terrains [1], providing significant benefits across various applications, including search and rescue, exploration, and assistive robotics. However, a major challenge in legged robot locomotion is maintaining stability and robustness in the presence of external disturbances and model uncertainties, such as uneven ground [2]–[4], unforeseen external forces, or heavy payloads [5]. These disturbances can severely impact the robot’s state, causing deviations from the desired trajectory and ultimately undermining both performance and stability.

To improve the stability and robustness of legged robots, various disturbance rejection methods have been developed and implemented. One approach involves designing sophisticated controllers, such as limit cycle walkers [6] and high-performance optimal control [7], [8]. In [7], a novel methodology for integrating adaptive control into a force-based control system was proposed for agile-legged robots. In [9], a min-max optimization model based on robust optimization was formulated, and a robust min-max model predictive controller was proposed to address quadruped locomotion control under uncertainties, specifically uncertain friction constraints and model dynamics. In [10], a two-level framework consisting of high-level and low-level control was proposed for robust payload transportation by quadrupedal robots. These methods effectively tackle model uncertainties in quadruped robots during payload transportation, especially those associated with

the single rigid body model. Another approach leverages disturbance rejection observers to further strengthen the robot’s robustness. In [11], a control framework for legged robots that enables self-perception and resilience to external disturbances was introduced, integrating a novel proprioceptive-based disturbance estimator that offers significant advantages in filtering foot-ground interaction noise and preventing the accumulation of estimation errors. In [12], a discrete-time generalized-momentum disturbance observer is used to enhance proprioceptive force control estimates, which are then combined with contact priors using Kalman Filtering for greater robustness. The generalized-momentum disturbance observer effectively estimates external disturbances in legged systems, but it encounters challenges when dealing with model uncertainties, particularly in robots with significant friction and complex dynamic interactions [13]. Similar to model uncertainties and external disturbances, fault conditions also reduce the robustness of legged robots due to susceptibility to various factors. Previous work on fault-tolerant locomotion in legged robots can be broadly classified into trajectory planning [14] and learning-based approaches [15]. However, few instances have been found where estimators are used to address fault tolerance in legged robots, due to the limited application of full-state observers, despite the widespread use of estimators to improve fault tolerance [16], [17].

The work in [13] proposed a two-level whole-body disturbance rejection control framework (WB-DRC) that integrates an extended state observer (ESO) with adaptive control and a moving horizon filter (MAF) to estimate uncertainties. This framework provides an opportunity to enhance fault tolerance capability in legged robots by utilizing a full-state estimator. The framework compensates for these uncertainties in the low-level control by solving a quadratic programming (QP) optimization problem, simultaneously addressing fault tolerance, model uncertainties, and external disturbances in legged systems. However, due to the sensitivity of the ESO to noise [18], [19], the performance of the adaptive ESO in estimating uncertainties within the WB-DRC is compromised as noise increases, particularly with the adoption of a larger moving horizon window in the MAF or a smaller ESO bandwidth. If uncertainty estimation performance is not compromised, the QP problem may still become infeasible due to the influence of noise.

In this paper, we propose a three-level framework that incorporates a full-state feedback estimator and a single processing module at the mid-level to estimate uncertainties in legged systems, addressing model uncertainties, external disturbances,

and faults. This framework can include not only the ESO but also other full-state estimators, such as predefined-time observers and model reference adaptive estimators to estimate the uncertainties in legged systems. Furthermore, to mitigate the impact of noise on the legged system, we propose a MH-ESO, which is less sensitive to noise than the ESO, to act as the full-state estimator within the three-level framework. A robust model predictive control, which is less sensitive to noise than QP solving, is adopted to plan the trajectories of dynamics with uncertainties for low-level control. The main contributions and important emphases are the following:

1) A three-level whole-body disturbance rejection control framework is proposed to enhance the robustness of legged robots in the presence of model uncertainties, external disturbances, and faults. Full-state feedback estimators, including ESO and MH-ESO, can be employed within the framework to estimate uncertainties in legged robots, which are hybrid systems. Additionally, commonly used filters for smoothing interaction noise, such as MAF and low-pass filters, can be incorporated into the framework.

2) A moving horizon extended state observer, which is less sensitive to noise than the ESO, is proposed. The moving horizon extended state observer's fast computation is achieved by solving the linear equation.

3) Simulations are conducted on both humanoid and quadruped robots, and experiments are performed on the Unitree A1 quadruped robot to validate the effectiveness of the proposed T-WB-DRC, highlighting its advantages in robustness and stability.

This paper is organized as follows. Section II provides background information on legged robots. Section III presents the high-level control approach. Section IV introduces the uncertainties estimator. Section V presents the robust model predictive control. Section VI provides the low-level control. Sections VII and VIII assess the performance of the framework through simulations and experimental verification, respectively. Finally, Section IX concludes the paper.

II. PRELIMINARIES

A legged robot is a free-floating-base system composed of $6 + n$ degrees of freedom

$$D(q)\ddot{q} + C(q, \dot{q})\dot{q} + G(q) = S^\top \tau + J(q)^\top F + d \quad (1)$$

where $q = [(q^b)^\top, (q^j)^\top]^\top$ with $q^b \in \mathbb{R}^6$, $D(q) : \mathbb{R}^{6+n} \rightarrow \mathbb{R}^{(6+n) \times (6+n)}$ is a positive definite inertia matrix, $C(\dot{q}, q) : \mathbb{R}^{6+n} \times \mathbb{R}^{6+n} \rightarrow \mathbb{R}^{(6+n) \times (6+n)}$ is the Coriolis matrix, $G(q) : \mathbb{R}^{6+n} \rightarrow \mathbb{R}^{6+n}$ is the gravity vector; $S = [0_{n \times 6} \quad I_n]$ is the actuated part selection matrix; $\tau \in \mathbb{R}^n$ is the actuation torques; $F \in \mathbb{R}^{3n_c}$ is the ground reaction forces (GRFs) of the stance leg; $J \in \mathbb{R}^{3n_c \times (6+n)}$ is the Jacobians that transposes the GRFs into the acceleration of the base and the actuated joints; $d \in \mathbb{R}^{n+6}$ is the system uncertainty; n and n_c represent the number of active degrees of freedom and the number of legs on the support surface, respectively.

We denote h as the linear momentum and L as the angular momentum around the robot's center of mass (CoM). Denoting $c \in \mathbb{R}^3$ as the position of the CoM in the inertial frame, and $h = mc\dot{c}$ denotes the linear momentum, where m is the total mass of the robot. The centroidal momentum is linked to the

joint configuration and its derivatives through the centroidal mapping

$$\begin{bmatrix} \dot{h} \\ \dot{L} \end{bmatrix} = A(q)\dot{q} \quad (2)$$

with $A(q)$ being the so-called centroidal momentum matrix [20]. The centroidal dynamics [21] can be obtained according to the Newton-Euler law:

$$\begin{aligned} \dot{h} &= \sum_{i=1}^{n_c} f_i - mg \\ \dot{L} &= \sum_{i=1}^{n_c} (p_i - c) \times f_i \end{aligned} \quad (3)$$

where $f_i \in \mathbb{R}^3$ represents the contact force of contact i , p_i denotes the position of contact i , and $g = [0, 0, 9.81]^\top$ is the gravity vector. The centroidal dynamics (3) is referred to as the nominal centroidal dynamics, where the force f_i is considered only as the ground reaction force, with external forces neglected, and m represents the robot's nominal mass, excluding model uncertainties.

The legged robot's control system consists of several modules, including a two-level control (high-level control and low-level control), state estimation, and gait scheduler [22], as presented in Fig. 1. A reference trajectory can be generated for high-level control based on user input and state estimation. The gait scheduler determines the timing and sequence of the gait, coordinating the transition between the swing and stance phases of each leg. The high-level control module manages the position of the swing legs and the optimal GRFs for the stance legs, all in accordance with the user commands and gait timing. These components of the control architecture are detailed in [22]–[24].

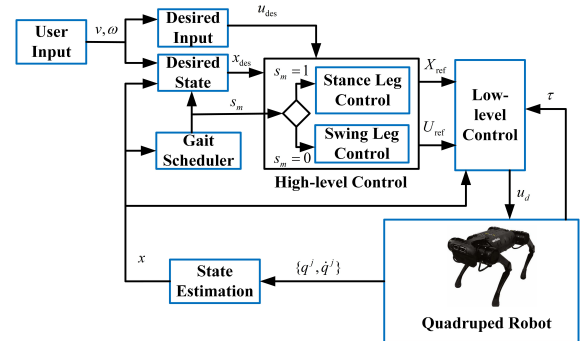


Fig. 1: A block diagram of a typical two-level control framework for legged robots.

To address the uncertainties and noise in legged robots, we propose a three-level whole-body disturbance rejection control architecture, as illustrated in Fig. 2. We employ model predictive control (MPC) in high-level control to plan the legged robot's centroidal momentum, joint positions, joint velocities, and GRFs based on nominal centroidal dynamics. The MH-ESO in mid-level control estimates disturbances and addresses noise in the legged system, while the MPC is used in mid-level control to replan the robot's joint acceleration and GRFs, based on the reference trajectory from high-level control and accounting for uncertainties. Finally, whole-body control in low-level control compensates for system disturbances.

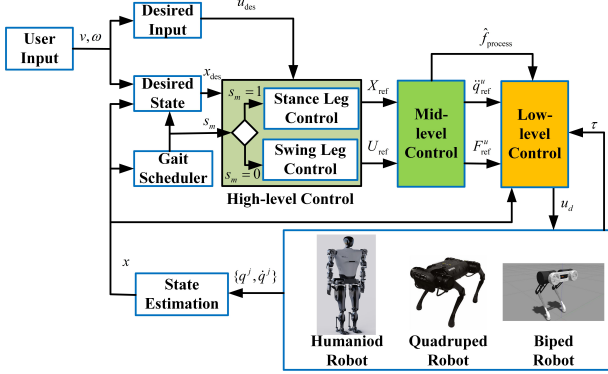


Fig. 2: Block diagram of the proposed T-WB-DRC.

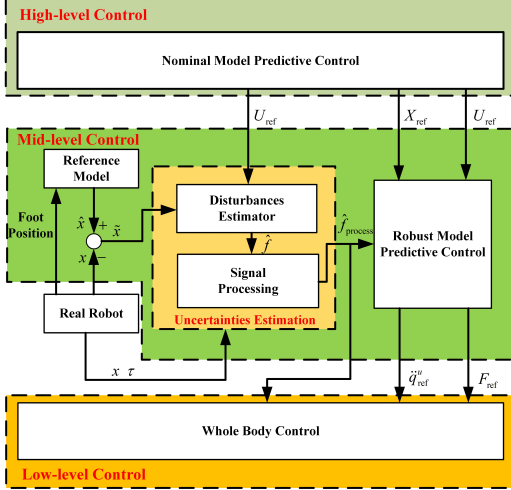


Fig. 3: Block diagram of three-level control in T-WB-DRC.

III. HIGH-LEVEL CONTROL

The high-level control employs MPC to generate reference trajectories for the GRFs, the robot's joint positions, joint velocities, and the centroidal momentum for the mid-level control. The same high-level control presented in [13] is adopted in this paper, and we revisit it in this section. We use the centroidal dynamics (3) for the high-level planning. Denote $x_c = [h^\top, L^\top, q^\top]^\top$, $u_c = [F^\top, (\dot{q}^j)^\top]^\top$ with $F = [f_1^\top, \dots, f_{n_c}^\top]^\top \in \mathbb{R}^{3n_c}$. The centroidal dynamics (3) can be rewritten as

$$\dot{x}_c = f_c(x_c, u_c) + d_c \quad (4)$$

where $d_c \in \mathbb{R}^{12+n}$ accounts for the uncertainties in the centroidal dynamics. **The d_c represents the difference in uncertainties between the nominal centroidal dynamics and the centroidal dynamics with disturbances. The centroidal dynamics (4) represents the nominal centroidal dynamics when d_c is a zero vector.** The continuous dynamics (4) is discretized over intervals of the prediction horizon $[t, t + T]$ for the nonlinear trajectory optimization problem. We consider the total number of steps in the MPC to be H , and thus the duration of each discrete interval is $\delta_t = T/(H - 1)$. Define $J_c(x)$ as the terminal quadratic cost around the reference state x_{des}

$$J_c(x) = (x - x_{\text{des}}(T))^\top Q_t (x - x_{\text{des}}(T)) \quad (5)$$

and $\varphi_c(x, u)$ as the quadratic cost around the reference state x_{des} and input u_{des}

$$\varphi_c(x, u) = (x - x_{\text{des}}(T))^\top Q_s (x - x_{\text{des}}(T)) + (u - u_{\text{des}}(T))^\top R (u - u_{\text{des}}(T)). \quad (6)$$

Let $x_{i,k}$ and $u_{i,k}$ denote the sequences of state and input variables in the MPC at the k -th solve, respectively, for $i = 1, \dots, H - 1$. The nonlinear MPC problem can be formulated by defining and evaluating a cost function and constraints as [10], [13]

$$\begin{aligned} \min_{X, U} \quad & J_c(x_{H,k}) + \sum_{i=0}^{H-1} \varphi_{c,i}(x_{i,k}, u_{i,k}) + l_i(x_{i,k}, u_{i,k}) \\ \text{s.t.} \quad & x_{0,k} - x_{m,k} = 0, \\ & x_{i+1,k} - x_{i,k} - f_c(x_{i,k}, u_{i,k})\delta t = 0, \\ & g_i(x_{i,k}, u_{i,k}) = 0, \quad i = 0, \dots, H - 1. \end{aligned} \quad (7)$$

where $x_{m,k}$ is the current measured state, $X = [x_{0,k}^\top, \dots, x_{H,k}^\top]^\top$ and $U = [u_{0,k}^\top, \dots, u_{H-1,k}^\top]^\top$ are the sequences of state and input variables respectively. The penalized cost function l_i is derived from inequality constraints, which ensure that the swing leg remains above the ground and that the contact force lies within the friction cone. The constraint function g_i represents the equality requirements, ensuring that the swing leg's end does not experience a contact force and that the end of the stance leg has zero velocity. Note that the legged robot is a hybrid system, where the f_i in the GRFs F is either a zero vector or a nonzero vector, with this being managed by the gait scheduler.

The solution to the MPC problem (7) is denoted as $X = X_{\text{ref}} := [h_{\text{ref}}^\top, L_{\text{ref}}^\top, q_{\text{ref}}^\top]^\top$ and $U = U_{\text{ref}} := [F_{\text{ref}}^\top, (\dot{q}_{\text{ref}}^j)^\top]^\top$, which gives the reference signals at the discrete time instances $[t, t + \delta_t, \dots, t + T]^\top$. We can linearly interpolate the discrete reference signals to a continuous reference trajectory for the interval $[t, t + T]$. We use the nominal dynamics with d_c being a zero vector in the MPC problem (7), since we prefer to generate the reference trajectory as if the system does not encounter the disturbances.

IV. UNCERTAINTIES ESTIMATION

In this section, we introduce two disturbance estimators, ESO and MH-ESO, which is designed based on ESO, to estimate uncertainties in the legged system, as discussed in section IV-A. Both disturbance estimators can be adopted in our proposed T-WB-DRC framework. We also present the signal processing module in T-WB-DRC, as described in section IV-B.

A. Disturbance Estimator

We will begin by designing the ESO and then integrate it into the moving horizon estimation (MHE) process to effectively manage noise.

Let $x_1 = q$ and $x_2 = \dot{q}$. The dynamics model (1) can be written in the state-space form

$$\begin{bmatrix} \dot{x}_1 \\ \dot{x}_2 \end{bmatrix} = \begin{bmatrix} x_2 \\ f_e(x_1, x_2) \end{bmatrix} + \begin{bmatrix} 0 \\ g_e(x_1) \end{bmatrix} u + \begin{bmatrix} 0 \\ d_e \end{bmatrix} \quad (8)$$

where

$$\begin{aligned} d_e &:= D^{-1}(x_1)d \\ f_e(x_1, x_2) &:= -D^{-1}(x_1)(C(x_2, x_1)x_2 + G(x_1)) \\ g_e(x_1) &:= D^{-1}(x_1)B \end{aligned}$$

with $B = [S^\top, J(x_1)^\top]^\top$ and $u = [\tau^\top, F^\top]^\top$.

1) *ESO design:* We extend the state $x_3 \in \mathbb{R}^{6+n}$. Let $x_3 = d_e$ and $h_x(t)$ denote the rate of change of uncertainty, i.e., $h_x(t) = \dot{x}_3$, both x_3 and $h_x(t)$ are assumed to be unknown but bounded vector functions. The system (8) can be expressed in state-space form as

$$\begin{cases} \dot{x}_1 = x_2 \\ \dot{x}_2 = f_e(x_1, x_2) + g_e(x_1)u + x_3 \\ \dot{x}_3 = h_x(t) \end{cases} \quad (9)$$

Let \hat{x}_1, \hat{x}_2 , and \hat{x}_3 be the estimates of x_1, x_2 , and x_3 , respectively. Referring to [25], the linear ESO can be constructed as follows

$$\begin{cases} \dot{\hat{x}}_1 = \hat{x}_2 + 3\omega_0(x_1 - \hat{x}_1) \\ \dot{\hat{x}}_2 = f_e(x_1, x_2) + g_e(x_1)\hat{u} + \hat{x}_3 + 3\omega_0^2(x_1 - \hat{x}_1) \\ \dot{\hat{x}}_3 = \omega_0^3(x_1 - \hat{x}_1) \end{cases} \quad (10)$$

where $\hat{u} = [\tau^\top, F_{\text{ref}}^\top]^\top$ with F_{ref} obtained by solving the MPC problem (7) and ω_0 is tuning parameter to be determined. We use F_{ref} in \hat{u} as the system input to estimate the system uncertainties. The discrepancy between F and F_{ref} is estimated using the ESO.

Next, we analyze the stability of the linear ESO. Let

$$\eta = [(x_1 - \hat{x}_1)^\top, (x_2 - \hat{x}_2)^\top / \omega_0, (x_3 - \hat{x}_3)^\top / \omega_0^2]^\top \quad (11)$$

be the state estimation error and $\tilde{u} = u - \hat{u}$. The dynamics of the state estimation errors can be expressed as

$$\dot{\eta} = \omega_0 A \eta + \frac{C_1 g_e(x_1) \tilde{u}}{\omega_0} + \frac{C_2 h_x(t)}{\omega_0^2} \quad (12)$$

where \tilde{u} is an unknown but a bounded vector, since $\|\tilde{u}\| = \|F - F_{\text{ref}}\|$, with F_{ref} being bounded as a result of solving MPC problem (7), $g_e(x_1)$ is a bounded matrix, and

$$\begin{aligned} A &= \begin{bmatrix} -3 & 1 & 0 \\ -3 & 0 & 1 \\ -1 & 0 & 0 \end{bmatrix} \otimes I_{6+n}, \\ C_1 &= \begin{bmatrix} 0 & 1 & 0 \end{bmatrix}^\top \otimes I_{6+n}, \\ C_2 &= \begin{bmatrix} 0 & 0 & 1 \end{bmatrix}^\top \otimes I_{6+n}. \end{aligned} \quad (13)$$

Note that the matrix A is Hurwitz.

Assumption 4.1: The error vector $g_e \tilde{u}$ is bounded, i.e., $\|g_e \tilde{u}\| \leq \tilde{u}_b$, where \tilde{u}_b is a constant. ■

Remark 4.1: The matrix g_e given in (8) is bounded because the inverse of the inertia matrix D^{-1} and the Jacobians J are both bounded when the legged robots operate within the workspace [26]. If the legged robot operates without uncertainty, and the robot's position q and velocities \dot{q} perfectly track q_{ref} and \dot{q}_{ref} , then \hat{u} will be equal to u , i.e., $\|\tilde{u}\| = 0$. This implies that Assumption 4.1 is not a strict requirement, especially when the uncertainties are small. ■

Theorem 4.1: Consider the error dynamics (12) under Assumption 4.1. Suppose both the disturbance x_3 and its derivative $h_x(t)$ are bounded, i.e., $\|x_3\| \leq d_b$ and $\|h_x(t)\| \leq h_b$, then the estimation error η is bounded. ■

Proof: Let us consider the following control Lyapunov candidate function:

$$V(\eta) = \eta^\top P \eta \quad (14)$$

where the matrix P satisfies $A^\top P + PA = -I$. Therefore, its time derivative will be

$$\begin{aligned} \dot{V}(\eta) &= -\omega_0 \eta^\top \eta + \frac{\tilde{u}^\top g_e^\top C_1^\top P \eta + \eta^\top P C_1 g_e \tilde{u}}{\omega_0} \\ &\quad + \frac{h_x^\top C_2^\top P \eta + \eta^\top P C_2 h_x}{\omega_0^2}. \end{aligned} \quad (15)$$

It follows that

$$\dot{V}(\eta) \leq -\omega_0 \|\eta\|^2 + \left(\frac{2u_b \|C_1^\top P\|}{\omega_0} + \frac{2h_b \|C_2^\top P\|}{\omega_0^2} \right) \|\eta\|. \quad (16)$$

From (14), we have

$$V(\eta) \leq \lambda_{\max}(P) \|\eta\|^2. \quad (17)$$

Let $\lambda = \omega_0 / 2\lambda_{\max}(P)$. Combining (16) and (17), we have

$$\dot{V}(\eta) + \lambda V(\eta) \leq a(\|\eta\| + \frac{b}{2})^2 + \lambda \delta_V \quad (18)$$

where

$$\begin{aligned} a &= -\omega_0 + \lambda \lambda_{\max}(P), \quad b = 2 \left(\frac{u_b \|C_1^\top P\|}{\omega_0} + \frac{h_b \|C_2^\top P\|}{\omega_0^2} \right) / a, \\ \delta_V &= \frac{(\omega_0 u_b \|C_1^\top P\| + h_b \|C_2^\top P\|)^2}{a \lambda \omega_0^4}. \end{aligned}$$

From (18), we have

$$\dot{V}(\eta) + \lambda V(\eta) \leq \lambda \delta_V. \quad (19)$$

Invoking the comparison lemma [27] for (19) yields

$$V(\eta) \leq V(\eta_0) \exp(-\lambda t) + \delta_V (1 - \exp(-\lambda t)) \quad (20)$$

where η_0 is the values of η .

Since $V(\eta) \geq \lambda_{\min}(P) \|\eta\|^2$, with $\lambda_{\min}(P)$ being the minimum eigenvalue of matrix P , it follows that

$$\|\eta\| \leq \sqrt{\frac{V(\eta_0) \exp(-\lambda t) + \delta_V (1 - \exp(-\lambda t))}{\lambda_{\min}(P)}}. \quad (21)$$

Thus, the estimation error η is bounded. ■

By adopting the ESO, the estimated uncertainties \hat{f} of legged robots are given by

$$\hat{f} = D(x_1) \hat{x}_3. \quad (22)$$

2) *MH-ESO design*: Denote y_1 and y_2 as the measurements of the position and velocity, respectively. That is,

$$\begin{aligned} y_1 &= x_1 + \eta_{\text{pos}} \\ y_2 &= x_2 + \eta_{\text{vel}} \end{aligned} \quad (23)$$

where η_{pos} and η_{vel} represent the position and velocity measurement noise, respectively.

Since the states x_1 and x_2 cannot be measured directly, we express the linear ESO in (10) as follows:

$$\begin{cases} \dot{\hat{x}}_1 = \hat{x}_2 + 3\omega_0(y_1 - \hat{x}_1) + w_1 \\ \dot{\hat{x}}_2 = f_e(y_1, y_2) + g_e(y_1)\hat{u} + \hat{x}_3 + 3\omega_0^2(y_1 - \hat{x}_1) + w_2 \\ \dot{\hat{x}}_3 = \omega_0^3(y_1 - \hat{x}_1) + w_3 \end{cases} \quad (24)$$

where

$$\begin{aligned} w_1 &= -3\omega_0\eta_{\text{pos}} \\ w_2 &= f_e(x_1, x_2) - f_e(y_1, y_2) + (g_e(x_1) - g_e(y_1)) - 3\omega_0^2\eta_{\text{pos}} \\ w_3 &= -\omega_0^3\eta_{\text{pos}}. \end{aligned}$$

Assumption 4.2: $f_e(x_1, x_2) : \mathbb{R}^{6+n} \times \mathbb{R}^{6+n} \rightarrow \mathbb{R}^{6+n}$ is globally Lipschitz continuous with respect to $[x_1^\top, x_2^\top]^\top$. For any two constant vector $a = [a_1^\top, a_2^\top]^\top \in \mathbb{R}^{12+2n}$ and $b = [b_1^\top, b_2^\top]^\top \in \mathbb{R}^{12+2n}$, f_e satisfies

$$\|f_e(a_1, a_2) - f_e(b_1, b_2)\| \leq \gamma_1 \|a - b\|.$$

where $\gamma_1 > 0$ represents the Lipschitz constant. ■

Assumption 4.3: $g_e(x_1) : \mathbb{R}^{6+n} \rightarrow \mathbb{R}^{6+n}$ is globally Lipschitz continuous with respect to x_1 . For any two constant vector $a_3, b_3 \in \mathbb{R}^{6+n}$, g_e satisfies

$$\|g_e(a_3) - g_e(b_3)\| \leq \gamma_2 \|a_3 - b_3\|.$$

where $\gamma_2 > 0$ represents the Lipschitz constant. ■

Under Assumptions 4.2 and 4.3, the vector w_2 is bounded, given that the noise terms η_{pos} and η_{vel} are bounded, and the stability of the ESO in (10) is equivalent to the stability of the ESO in (24). The difference between (10) and (24) lies in that the feedback signals y_1 and y_2 in (24) can be measured directly, while $w = [w_1^\top, w_2^\top, w_3^\top]^\top$ can be obtained optimally using the following MHE.

Specifically, we employ MHE to estimate the state \hat{x} in (24) and deal with the noise w . Let

$$z(k) = [\hat{x}_1^\top(k), \hat{x}_2^\top(k), \hat{x}_3^\top(k)]^\top.$$

The ESO in (24) can be discretized using the backward Euler formula, yielding as

$$z(k+1) = A_0 z(k) + u_z(k) + w_t \quad (25)$$

where $A_0 = \bar{A}_0 - L_0 C_0$ and

$$u_z(k) = B_0 [f_e(y_1(k), y_2(k)) + g_e(y_1(k))\hat{u}(k)] + L_0 y_1(k)$$

with t_s being the sampling period and

$$\begin{aligned} \bar{A}_0 &= \begin{bmatrix} 1 & t_s & 0 \\ 0 & 1 & t_s \\ 0 & 0 & 1 \end{bmatrix} \otimes I_{6+n}, \\ B_0 &= \begin{bmatrix} 0 & t_s & 0 \end{bmatrix}^\top \otimes I_{6+n}, \\ C_0 &= \begin{bmatrix} 1 & 0 & 0 \end{bmatrix} \otimes I_{6+n}, \\ L_0 &= \begin{bmatrix} 3\omega_0 t_s & 3\omega_0^2 t_s & \omega_0^3 t_s \end{bmatrix}^\top \otimes I_{6+n}. \end{aligned}$$

The $u_z(k)$ is considered as the system input for the discrete system (25), with $y_1(k)$, $y_2(k)$, and $\hat{u}(k)$ either being directly measured or obtained through state estimation.

Let

$$y(k) = [y_1^\top(k), y_2^\top(k), 0_{6+n}^\top]^\top$$

represent the measurement data used for solving the subsequent MHE problem. At each step $k = N, N+1, \dots$, the goal of MHE is to estimate state $z(k-N|k)$ in (25) as $\hat{z}(k-N|k)$, based on the past measurement data $y_{k-N}^k = \text{col}(y(k-N), \dots, y(k))$, the past input $u_{k-N}^{k-1} = \text{col}(u_z(k-N), \dots, u_z(k-1))$, and the prediction state $\bar{z}(k-N|k)$ for $z(k-N)$, where N is the moving horizon size. Consider the following cost function:

$$\begin{aligned} J(k) &= \|\hat{z}(k-N|k) - \bar{z}(k-N|k)\|_\Gamma^2 + \sum_{i=k-N}^{k-1} \|\hat{w}(i|k)\|_\Lambda^2 \\ &+ \sum_{i=k-N}^k \|y(i) - \hat{y}(i|k)\|_\Pi^2. \end{aligned} \quad (26)$$

Then, at each step $k = N, N+1, \dots$, the following MHE optimization problem is solved.

Problem 1: Given a triplet $\{\bar{z}(k-N|k), y_{k-N}^k, u_{k-N}^{k-1}\}$, find the optimal estimate $\hat{z}(k-N|k)$ and $\hat{w}_{k-N|k}^{k-1|k}$ that

$$\min_{\hat{z}(k-N|k), \hat{w}_{k-N|k}^{k-1|k}} J(k) \quad (27)$$

with the optimal prediction \bar{z} in $J(k)$ is determined as

$$\begin{aligned} \bar{z}(0|N) &= \bar{z}(0) \\ \bar{z}(j+1|k) &= A_0 \bar{z}(j|k) + u_0(j) + \hat{w}(j|k-1) \\ j &= k-N-1, \dots, k-2, k-1, \end{aligned} \quad (28)$$

and the following constraints are satisfied

$$\begin{aligned} \hat{z}(i+1|k) &= A_0 \hat{z}(i|k) + u_0(i) + \hat{w}(i|k) \\ \hat{y}(i|k) &= C_0 \hat{z}(i|k). \end{aligned} \quad (29)$$

Theorem 4.2: Given a triplet $\{\bar{z}(k-N|k), y_{k-N}^k, u_{k-N}^{k-1}\}$, the solution to Problem 1 is given by

$$\begin{aligned} \hat{z}(k-N|k) &= (\Gamma + M_1)^{-1} [M_2 y_{k-N}^k + \Gamma \bar{z}(k-N|k) \\ &\quad - M_2 H_N u_{k-N}^{k-1}] \\ \hat{w}_{k-N|k}^{k-1|k} &= M_3^{-1} \Pi H_N^\top [y_{k-N}^k - F_N \hat{z}(k-N|k) \\ &\quad - H_N u_{k-N}^{k-1}] \end{aligned} \quad (30)$$

$$\quad (31)$$

where $M_1 = \Pi F_N^\top [I - \Pi H_N M_3^{-1} H_N^\top] F_N$, $M_2 = \Pi F_N^\top [I - \Pi H_N M_3^{-1} H_N^\top]$, $M_3 = \Lambda + \Pi H_N^\top H_N$ with

$$F_N = \begin{bmatrix} C_0 \\ C_0 A_0 \\ C_0 A_0^2 \\ \vdots \\ C_0 A_0^N \end{bmatrix}, H_N = \begin{bmatrix} 0 & 0 & \cdots & 0 \\ C_0 & 0 & \cdots & 0 \\ C_0 A_0 & C_0 & \ddots & \vdots \\ \vdots & \vdots & \ddots & 0 \\ C_0 A_0^{N-1} & C_0 A_0^{N-2} & \cdots & C_0 \end{bmatrix}.$$

Proof: From (29), the optimal observation vectors $\hat{y}_{k-N}^k = \text{col}(\hat{y}(k-N), \dots, \hat{y}(k))$ can be written as follows:

$$\hat{y}_{k-N}^k = F_N \hat{z}(k-N) + H_N u_{k-N}^{k-1} + H_N \hat{w}_{k-N}^{k-1}. \quad (32)$$

Substituting (32) into (26) gives

$$J(k) = \|\hat{z}(k-N|k) - \bar{z}(k-N|x)\|_\Gamma^2 + \|\hat{w}_{k-N|k}^{k-1}\|_\Lambda^2 + \|F_N \hat{z}(k-N|k) + H_N u_{k-N}^{k-1} + H_N \hat{w}_{k-N|k}^{k-1} - y_{k-N}^k\|_\Pi^2.$$

The necessary condition for the minimum of the cost function $J(k)$ is given by

$$\frac{\partial J(k)}{\partial \hat{z}(k-N|k)} = 0, \quad \frac{\partial J(k)}{\partial \hat{w}_{k-N|k}^{k-1}} = 0. \quad (33)$$

From (33), the following partial differential equations can be derived

$$\begin{aligned} \frac{\partial J(k)}{\partial \hat{z}(k-N|k)} &= 2\Gamma[\hat{z}(k-N|k) - \bar{z}(k-N|x)] \\ &+ 2\Pi F_N^\top [F_N \hat{z}(k-N|k) + H_N \hat{w}_{k-N}^{k-1} + H_N \hat{w}_{k-N|k}^{k-1} - y_{k-N}^k] \\ \frac{\partial J(k)}{\partial \hat{w}_{k-N|k}^{k-1}} &= 2\Lambda \hat{w}_{k-N|k}^{k-1} \\ &+ 2\Pi H_N^\top [F_N \hat{z}(k-N|k) + H_N \hat{w}_{k-N}^{k-1} + H_N \hat{w}_{k-N|k}^{k-1} - y_{k-N}^k]. \end{aligned} \quad (34)$$

Combining (33) and (34), it gives

$$\begin{aligned} \hat{z}(k-N|k) &= (\Gamma + \Pi F_N^\top F_N)^{-1} [\Pi F_N^\top y_{k-N}^k - \Pi F_N^\top H_N u_{k-N}^{k-1} \\ &+ \Gamma \bar{z}(k-N|x) - \Pi F_N^\top H_N \hat{w}_{k-N|k}^{k-1}] \\ \hat{w}_{k-N|k}^{k-1} &= (\Lambda + \Pi H_N^\top H_N)^{-1} [\Pi H_N^\top y_{k-N}^k \\ &- \Pi H_N^\top F_N \hat{z}(k-N|k) - \Pi H_N^\top H_N u_{k-N}^{k-1}]. \end{aligned} \quad (35)$$

The result in (31) can be derived from (35). The proof is completed. ■

Then, the estimated uncertainties \hat{f} using MH-ESO are given by

$$\hat{f} = D(y_1) \hat{z}_3(k-N|k) \quad (36)$$

where $z_3(k-N|k)$ represents the bottom $6+n$ elements of $\hat{z}(k-N|k)$.

Remark 4.2: The two equations in (35) can be expressed as a system of linear equations

$$N_1 d_{\text{opt}} = N_2 \quad (37)$$

where $d_{\text{opt}} = \text{col}(\hat{z}(k-N|k), \hat{w}_{k-N|k}^{k-1})$,

$$N_1 = \begin{bmatrix} \Gamma + \Pi F_N^\top F_N & \Pi F_N^\top H_N \\ \Pi H_N^\top F_N & \Lambda + \Pi H_N^\top H_N \end{bmatrix} \\ N_2 = \begin{bmatrix} \Pi F_N^\top y_{k-N}^k - \Pi F_N^\top H_N u_{k-N}^{k-1} + \Gamma \bar{z}(k-N|x) \\ \Pi H_N^\top [y_{k-N}^k - H_N u_{k-N}^{k-1}] \end{bmatrix}.$$

In practical applications, to reduce the computation time for solving Problem 1, we do not need to obtain d_{opt} using the conclusion in Theorem 4.2 by inverting matrices, but instead can use the sparse LU decomposition method [28] to solve the linear equations (37). ■

Remark 4.3: The average computation time for the linear equation (37) increases as the MHE horizon N is set to a larger value. Table I presents the average computation time for the linear equation (37) corresponding to N , when the quadruped robot with $n = 12$ degrees of freedom is trotting in place, excluding model uncertainties. The test is conducted on a single computer with an Intel i7-13700KF processor at 3.4 GHz, and each test lasts for approximately 20 seconds.

TABLE I: The Average Computation Time

| N | Computation Time (ms) | N | Computation Time (ms) |
|---|-----------------------|----|-----------------------|
| 1 | 0.168153 | 8 | 5.42422 |
| 2 | 0.461572 | 10 | 8.21532 |
| 4 | 0.966662 | 12 | 19.9099 |
| 6 | 3.12035 | 14 | 27.229 |

Remark 4.4: The proposed MH-ESO has the advantage of suppressing the influence of measurement noise, especially when compared to the ESO, as presented in section VII-A. Other methods, such as adaptive control can also be used to estimate uncertainties and integrated into the proposed three-level framework to address uncertainties in legged robots, particularly when measurement noise can be neglected in the system. ■

B. Signal Processing

Note that the GRFs F_{ref} are used as the input to the system in (10) or (25), as opposed to the real robot's GRFs F . The discrepancy between F and F_{ref} is estimated using the estimator. This discrepancy transitions from zero to non-zero, or vice versa, as the GRFs F_{ref} and F transition from zero to non-zero, or vice versa. Since the discrepancy is estimated at high frequency, the estimated uncertainties undergo significant changes when the discrepancy transitions from zero to non-zero, or vice versa. To reduce noise caused by the interaction force switching, the MAF [11] and low-pass filter [7] can be used to mitigate the influence of interaction noise on the estimated uncertainties in legged robots. Additionally, we provide a saturator to limit the estimated uncertainties within a bounded range. Let

$$\hat{f}_{\text{process}} = \begin{cases} \alpha \hat{f} / \|\hat{f}\|, & \text{if } \|\hat{f}\| > \alpha \\ \hat{f}, & \text{otherwise} \end{cases} \quad (38)$$

denote the processed estimated uncertainties produced by the saturator. The saturator only bounds the input signal without introducing signal delay, unlike the MAF and low-pass filter.

Remark 4.5: The parameter α can be chosen according to the Frobenius norm of the estimated uncertainties \hat{f} when applied to robots standing in place without moving. For example, Fig. 4 shows the Frobenius norm of the uncertainties \hat{f} estimated by MH-ESO when the robot is standing in place while carrying a 10 kg load. The norm of the estimated uncertainties lies within the interval $[25, 70.1]$, so we can choose α to lie within this range to handle model uncertainties due to a 10 kg load or any load less than 10 kg. ■

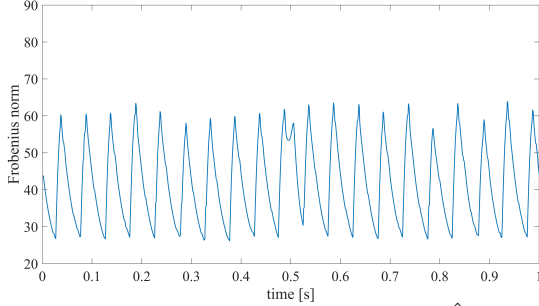


Fig. 4: Frobenius norm of the uncertainties \hat{f} estimated by MH-ESO when the robot, carrying a 10kg load, is standing in place.

V. ROBUST MODEL PREDICTIVE CONTROL

In this section, we employ a robust MPC based on centroidal dynamics with uncertainties to replan the GRFs reference trajectories for low-level control.

Due to the uncertainties are estimated in section IV based on whole-body dynamics, we first calculate the uncertainties in the centroidal dynamics using the uncertainties d derived from the whole-body dynamics (1). Note that the d_c represents the differences in uncertainties between the centroidal dynamics with disturbances and the nominal centroidal dynamics. The derivatives of centroidal momentum are obtained as [20]

$$\begin{bmatrix} \dot{h} \\ \dot{L} \end{bmatrix} = A(q)\ddot{q} + \dot{A}\dot{q}. \quad (39)$$

Then, the centroidal dynamics can be rewritten as

$$\dot{x}_c = \begin{bmatrix} \dot{h} \\ \dot{L} \\ \dot{q} \end{bmatrix} = f_h(q, \dot{q}, \ddot{q}). \quad (40)$$

where

$$f_h(q, \dot{q}, \ddot{q}) = \begin{bmatrix} A(q)\ddot{q} + \dot{A}\dot{q} \\ \dot{q} \end{bmatrix}. \quad (41)$$

Thus, the uncertainties d_c is

$$d_c = f_h(q, \dot{q}, \ddot{q}) - f_h(q_{\text{ref}}, \dot{q}_{\text{ref}}, \ddot{q}_{\text{ref}}). \quad (42)$$

It is noted that q_{ref} , \dot{q}_{ref} , \ddot{q}_{ref} are derived from the nominal MPC in high-level control.

Subsequently, we construct a robust MPC approach to determine the reference trajectories for the robot's GRFs,

while accommodating uncertainties. The continuous dynamics (3) are discretized over intervals of the prediction horizon $[t, t + T_0]$ for the formulation of the nonlinear MPC trajectory optimization problem. Choosing the time horizon of the MPC problem as $M - 1$, thus the discrete interval is set to $\delta t_0 = T_0/(M - 1)$. Define

$$J_u(x) = (x - X_{\text{ref}}(t))^\top Q_t^u (x - X_{\text{ref}}(t))$$

and

$$\varphi_u(x, u) = (x - X_{\text{ref}}(t))^\top Q_s^u (x - X_{\text{ref}}(t)) + (u - U_{\text{ref}}(t))^\top R (u - U_{\text{ref}}(t)).$$

where X_{ref} and U_{ref} are obtained by solving the nominal MPC problem in high-level control. Since the acceleration \ddot{q} in (40) cannot be measured directly, we obtain the acceleration estimation $\hat{\ddot{q}}$ as

$$\hat{\ddot{q}} = D(q)^{-1} (-C(q, \dot{q})\dot{q} - G(q) + S^\top \tau + J(q)^\top F_{\text{ref}} + \hat{f}_{\text{process}})$$

with \hat{f}_{process} being given in (38). From (42), the uncertainty estimate \hat{d}_c is given by

$$\hat{d}_c = f_h(q, \dot{q}, \hat{\ddot{q}}) - f_h(q_{\text{ref}}, \dot{q}_{\text{ref}}, \ddot{q}_{\text{ref}}). \quad (43)$$

The nonlinear robust MPC trajectory optimization problem can be formulated as

$$\begin{aligned} \min_{X, U} \quad & J_u(x_M) + \sum_{i=0}^{M-1} \varphi_{u,i}(x_k, u_k) + l_i(x_k, u_k) \\ \text{s.t.} \quad & x_{0,k} - x_{m,k} = 0, \\ & x_{i+1,k} - x_{i,k} - f_c(x_{i,k}, u_{i,k})\delta t_0 = \hat{d}_c, \\ & g_i(x_{i,k}, u_{i,k}) = 0, \quad i = 0, \dots, N-1. \end{aligned} \quad (44)$$

The solution to the MPC problem (44) is denoted as $X = X_{\text{ref}}^u := [(h_{\text{ref}}^u)^\top, (q_{\text{ref}}^u)^\top]^\top$ and $U = U_{\text{ref}}^u := [(F_{\text{ref}}^u)^\top, (\dot{q}_{\text{ref}}^{u,j})^\top]^\top$, corresponding to discrete time $[t, t + \delta t_0, \dots, t + M\delta t_0]^\top$. The reference velocity is given by

$$\dot{q}_{\text{ref}}^u = \begin{bmatrix} \dot{q}_{\text{ref}}^{u,b} \\ \dot{q}_{\text{ref}}^{u,j} \end{bmatrix}. \quad (45)$$

The reference velocity $\dot{q}_{\text{ref}}^{u,b}$ for the base can be obtained as

$$\dot{q}_{\text{ref}}^{u,b} = A_b^{-1}(q_{\text{ref}}^u) \left(\begin{bmatrix} h_{\text{ref}}^u \\ L_{\text{ref}}^u \end{bmatrix} - A_j(q_{\text{ref}}^u)\dot{q}_{\text{ref}}^{u,j} \right) \quad (46)$$

where $A(q)$ is partitioned as $A(q) := [A_b(q), A_j(q)]$ with $A_b(q) \in \mathbb{R}^{6 \times 6}$. Partition the matrix $D(q)$ in (1) as

$$D(q) = \begin{bmatrix} D_{11}(q) & D_{12}(q) \\ D_{21}(q) & D_{22}(q) \end{bmatrix} \quad (47)$$

where $D_{11}(q) \in \mathbb{R}^{6 \times 6}$. The reference acceleration vector for the actuated joints $\ddot{q}_{\text{ref}}^{u,j} \in \mathbb{R}^n$ is obtained by directly differentiating the joint velocity $\dot{q}_{\text{ref}}^{u,j}$. The base reference acceleration $\ddot{q}_{\text{ref}}^{u,b}$ for the base can be calculate as follows

$$\ddot{q}_{\text{ref}}^{u,b} = D_{11}(q_{\text{ref}}^u)^{-1} (S_\theta (-C(\dot{q}_{\text{ref}}^u, q_{\text{ref}}^u)\dot{q}_{\text{ref}}^u - G(q_{\text{ref}}^u) + J^\top F_{\text{ref}}^u) - D_{12}(q_{\text{ref}}^u)\ddot{q}_{\text{ref}}^{u,j}).$$

where $S_\theta = [I_6, 0_{6 \times n}]$. The reference acceleration is given by

$$\ddot{q}_{\text{ref}}^u = \begin{bmatrix} \ddot{q}_{\text{ref}}^{u,b} \\ \ddot{q}_{\text{ref}}^{u,j} \end{bmatrix}. \quad (48)$$

VI. LOW-LEVEL CONTROL

Similar to [13], we use the hierarchical WBC to address uncertainties in the legged system. The detailed formulation of WBC is presented in [29]. In WBC, each task is formulated with equality and inequality constraints on generalized accelerations, joint torques, and GRFs. Each task can be defined as a set of linear equality and inequality constraints. The hierarchical WBC can be formulated as

$$\begin{aligned}
 & \text{find } \ddot{q}_d, F_d, \tau_d \\
 & \text{s.t. } \underline{u} \leq u \leq \bar{u} \quad (\text{Task Torque limits}) \\
 & D(q)\ddot{q}_d + C(q, \dot{q})\dot{q} + G(q) = S^\top \tau_d + J^\top F_d + \hat{f}_{\text{process}} \quad (\text{Task Dynamics}) \\
 & J\ddot{q}_d + \dot{J}\dot{q} = 0 \quad (\text{Task No contact motion}) \\
 & C_f F_d \leq 0 \quad (\text{Task Friction cone}) \\
 & S_w F_d = 0 \quad (\text{Task No swing foot force}) \\
 & \ddot{q}_d - \ddot{q}_{\text{ref}}^u = 0 \quad (\text{Task Acceleration tracking}) \\
 & F_d - F_{\text{ref}}^u = 0 \quad (\text{Task Foot end force tracking})
 \end{aligned}$$

where \underline{u} and \bar{u} represent the lower and upper limits of the torque, q and \dot{q} are obtained by the feedback of the robot system, and J and \dot{J} are computed based on the gait and feedback. S_w is the swing leg selection matrix. Tasks are solved in a strictly prioritized order. The tasks used in the paper are described in Table II.

TABLE II: Each Task Is Associated With A Priority

| Priority | Task |
|----------|--|
| 1 | Dynamics + Friction cone + No swing foot force + Torque limits |
| 2 | Acceleration tracking |
| 3 | No contact motion + Foot end force tracking |

Finally, the actuation joint torque u_d can be computed using the PD control law as follows:

$$u_d = \tau_d^* + K_p(q_{\text{ref}}^{u,j} - q^j) + K_d(\dot{q}_{\text{ref}}^{u,j} - \dot{q}^j) \quad (49)$$

where τ_d^* is obtained by solving WBC problem, $K_p \in \mathbb{R}^{n \times n}$ and $K_d \in \mathbb{R}^{n \times n}$ are positive definite diagonal matrices of proportional and derivative gains, respectively. $q_{\text{ref}}^{u,j}$ and $\dot{q}_{\text{ref}}^{u,j}$ represent the bottom n elements of q_{ref}^u and \dot{q}_{ref}^u , respectively.

VII. SIMULATION VERIFICATION

To evaluate the effectiveness and versatility of the T-WB-DRC, we conduct a series of simulation experiments on legged robots. First, we present the advantages of the MH-ESO over the ESO. Second, we compare the performance of the proposed T-WB-DRC with the WB-DRC introduced in [13] and the widely adopted standard whole-body control framework (standard WB-C) from [10], considering model uncertainties, external disturbances, and fault tolerance.

All simulations are performed on a single PC (Intel i7-13700KF, 3.4 GHz). For the simulations, the control system is implemented using ROS Noetic in the Gazebo simulator. The simulations are carried out on both a humanoid robot (the upper body of the humanoid robot is modeled as a rigid body), which has $n = 12$ degrees of actuation freedom, and the

Unitree A1 quadruped robot, which also has $n = 12$ degrees of actuation freedom. For the T-WB-DRC, the high-level control, MH-ESO, robust MPC in mid-level control, and low-level control operate in four distinct threads. In contrast, for the WB-DRC and standard WB-C, the high-level control and low-level control are executed in two different threads. We select the same operating frequency for high-level control across all three methods, as well as the same operating frequency for low-level control.

A. Impact of Noise on ESO and MH-ESO

To show the MH-ESO and ESO sensitivity to noise, we introduced Gaussian random noise $\mathcal{N}(0, 0.001)$ to each element in the real position q^{real} to simulate authentic running environments as

$$q = q^{\text{real}} + \mathcal{N}(0, 0.001). \quad (50)$$

We conduct a simulation on the robot carrying a 10 kg load and standing in place to compare the Mean Squared Error (MSE) and the variance of the Frobenius norm of the estimated uncertainties \hat{f} using MH-ESO and ESO. This comparison demonstrates the impact of noise on the estimated uncertainties using both MH-ESO and ESO while the robot remains stationary with the 10 kg load. The MSE and variance of the Frobenius norm of the estimated uncertainties are defined as

$$MSE = \frac{1}{N} \sum_{i=1}^N (\hat{y}_i - \bar{y}_i)^2, \quad Var = \frac{1}{N} \sum_{i=1}^N (\hat{y}_i - \rho)^2 \quad (51)$$

where \hat{y}_i and \bar{y}_i represent the norms of the estimated uncertainties obtained using position feedback with noise and the average norms of the estimated uncertainties obtained using position feedback without noise, respectively, for MH-ESO or ESO; ρ represents the sample mean norms of the estimated uncertainties obtained using position feedback with noise.

TABLE III: MH-ESO and ESO Setting

| Parameter | Value for MH-ESO | Value for ESO |
|------------|-------------------------------|---------------|
| ω_0 | 200 | 200 |
| N | 4 | \times |
| Γ | $10 \times I_{54 \times 54}$ | \times |
| Λ | $1 \times I_{54N \times 54N}$ | \times |
| Π | 0.01 | \times |

The MH-ESO and ESO settings are presented in Table III. The top figure of Fig. 5 shows that the Frobenius norms of the uncertainties estimated by MH-ESO and ESO are similar when the robot's position feedback is free from Gaussian random noise. The bottom figure of Fig. 5 shows the Frobenius norms of the estimated uncertainties for both methods, suggesting that MH-ESO is less sensitive to noise than ESO. The average MSE and variance results, presented in Table IV, indicate that MH-ESO enhances noise suppression capability compared to ESO when both observers are set to the same bandwidth.

TABLE IV: MSE and Variance Results

| Method | MSE | Var |
|--------|--------|---------|
| MH-ESO | 95.127 | 90.0257 |
| ESO | 2754.4 | 1190.3 |

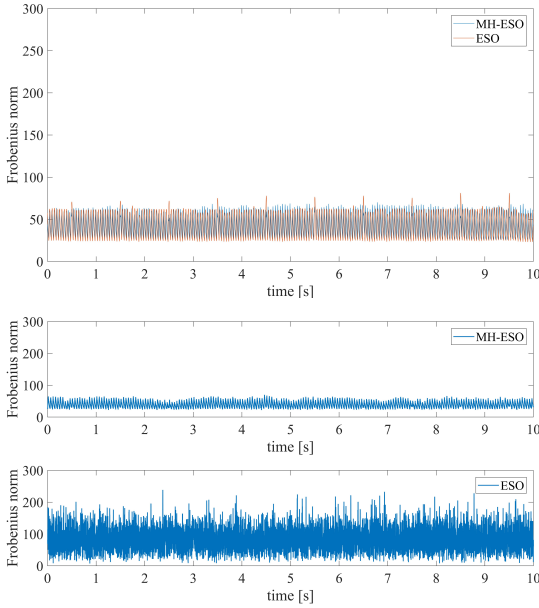


Fig. 5: The Frobenius norms of the uncertainties estimated by MH-ESO or ESO.

B. Simulations on Quadruped Robots

The operating frequency for high-level control is set to 20 Hz with the prediction horizon $T = 1s$ and the total number of steps $H = 50$, while the low-level control operates at 1000 Hz. The robust MPC also operates at 20 Hz with the prediction horizon $T_0 = 1s$ and the total number of steps $M = 50$. We select MH-ESO as the disturbance estimator to estimate uncertainties and use the saturator as the signal processing module, with the parameter $\alpha = 25$ set in the saturator. The operating frequency for MH-ESO is set to 1000 Hz, and the configuration of MH-ESO is provided in Table III. The desired base link (see Fig. 6) height is set to 0.31 m and the desired roll angles of the base link is set to 0 rad. To simulate realistic running environments, we introduced Gaussian random noise $\mathcal{N}(0, 0.001)$ to each element of the real position q^{real} , as shown in (50).

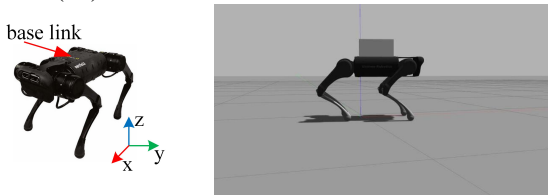


Fig. 6: The Unitree A1 robot (left) and its model in the simulation environment with a 10 kg load (right).

To demonstrate the effectiveness and versatility of T-WB-DRC, we conduct three simulation comparisons: (1) under model uncertainties with the robot carrying a 10 kg load, (2) under external disturbances with a constant force applied to the base link, and (3) to assess fault tolerance by reducing motor output torques. Fig. 7 illustrates the height of the base link over time as the robot, carrying a 10 kg load, walks at different velocities along the x -axis. The robot is commanded to move on the flat ground with velocities of -0.1 m/s, 0.1 m/s, 0.2 m/s, 0.4 m/s, and 0.6 m/s from 10 s to 60 s, each for a duration of 10 seconds. The results demonstrate that

the robot using T-WB-DRC maintains the body height closer to 0.31 m, showcasing its ability to effectively handle model uncertainties. Fig. 8 shows the height of the base link from the ground and the roll angle of the base link over time under the influence of various constant external forces. External forces of 20 N, -20 N, 40 N, -60 N, 80 N, and 80 N are applied to the base link along the z -axis, each for a duration of 10 seconds. The results demonstrate that the proposed T-WB-DRC compensates for these external disturbances better than the WB-DRC and the standard WB-C. Furthermore, we intentionally reduce the output torque of the robot's knee joint on the right back leg by 50% from 5s to 10s and by 90% from 19.8 s to 20 s to demonstrate the fault tolerance capability. The base link height of the robot while stepping in place is shown in Fig. 9 for T-WB-DRC, WB-DRC, and standard WB-C. For T-WB-DRC, under long-term motor output torque faults (from 5 s to 10 s), the height of the base link closely follows the desired trajectories, outperforming the robot using the standard WB-C and WB-DRC. In the case of short-term motor output torque faults (from 19.8 s to 20 s), the base link height of the robot using T-WB-DRC tracks the desired trajectories more rapidly compared to both the robot using the WB-DRC and the robot using standard WB-C. These results show that the robot using the WB-DRC exhibits better fault tolerance and enhanced robustness compared to the robot using the standard WB-C.

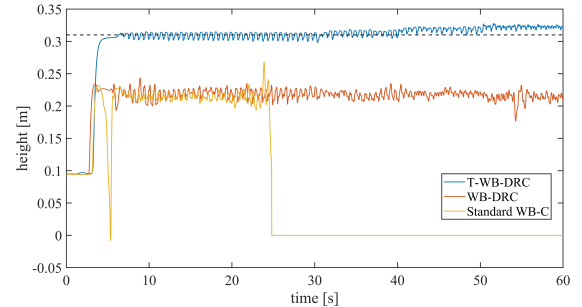


Fig. 7: The height of the base link of the robot when the robot moves carrying a 10 kg load.

C. Simulations on Humanoid Robots

The operating frequency for high-level control is set to 100 Hz with the prediction horizon $T = 1s$ and the total number of steps $H = 34$, while the low-level control operates at 1000 Hz. The robust MPC also operates at 100 Hz with the prediction horizon $T_0 = 1s$ and the total number of steps $M = 34$. The operating frequency for disturbances estimator is set to 1000 Hz. The desired base link height (see Fig. 10) is set to 0.80 m.

To demonstrate the fault tolerance capability of the humanoid robot, we intentionally reduce the output torque of the right leg's knee joint (see Fig. 10) by 30%. We select MH-ESO as the disturbance estimator to estimate uncertainties and use the MAF as the signal processing module, with the moving horizon window as 3. Fig. 11 and 12 show the height of the humanoid robot's base link when the knee joint motor's output torque is reduced by 30%, with the ESO bandwidth set to $\omega_0 = 100$ and $\omega_0 = 300$, respectively. Table V shows

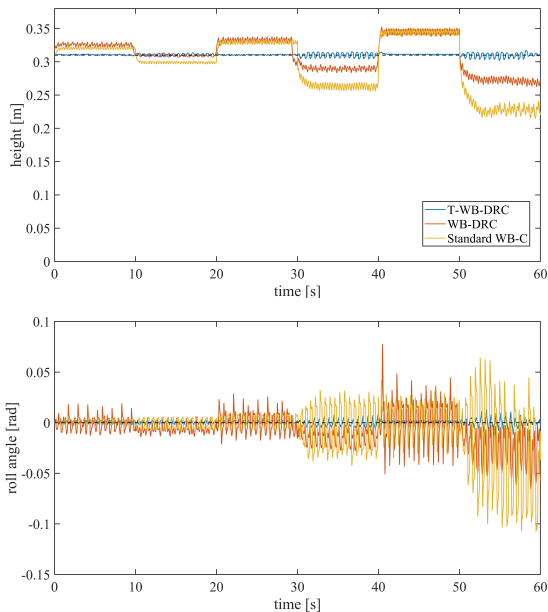


Fig. 8: The height and roll angle of the robot's base link when constant forces are applied to it.

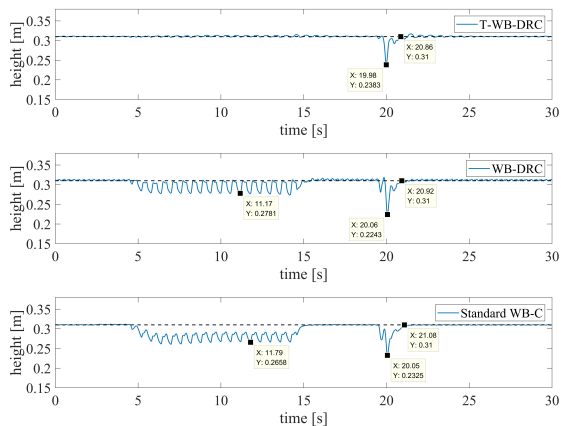


Fig. 9: The height of the robot's base link when the knee joint motor output torque is cut.

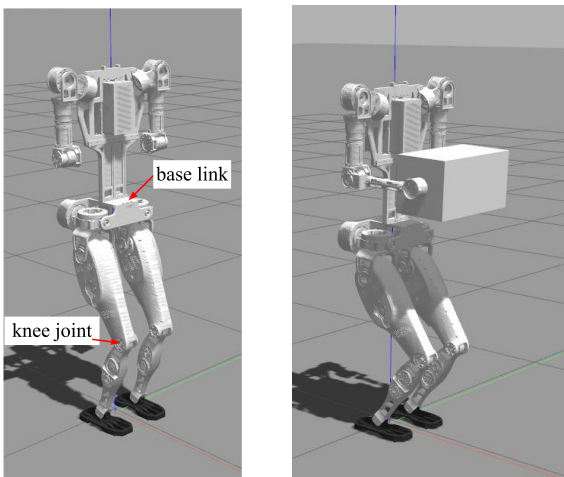


Fig. 10: The humanoid robot in the simulation environment (left) and the humanoid robot carrying a 8 kg load (right).

the MSE of the humanoid robot's base link height relative to the desired base link height. These results illustrate that the T-WB-DRC has the better fault tolerance capability than WB-DRC when the ESO bandwidth $\omega_0 = 100$. As shown in Fig. 12, the robot falls at the start of controller operation due to the increased noise influence as the ESO bandwidth is increased. This demonstrates that the T-WB-DRC has the potential to achieve better locomotion performance than WB-DRC, particularly in the presence of noise.

TABLE V: MSE of of Actual Height Relative to Desired Height

| Method | MSE ($\omega_0 = 100$) | MSE ($\omega_0 = 300$) |
|--------|--------------------------|--------------------------|
| MH-ESO | 1.6673e-04 | 1.8417e-04 |
| ESO | 3.2156e-04 | × |

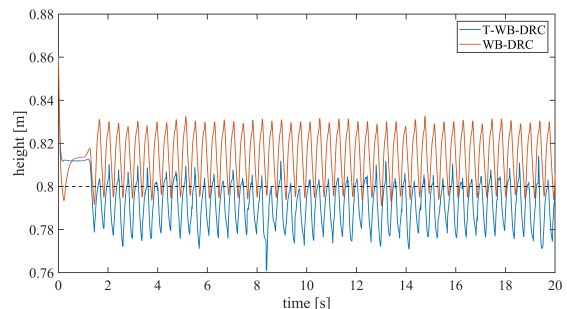


Fig. 11: The height of the humanoid robot's base link when the knee joint motor output torque is cut by 30% with $\omega_0 = 100$.

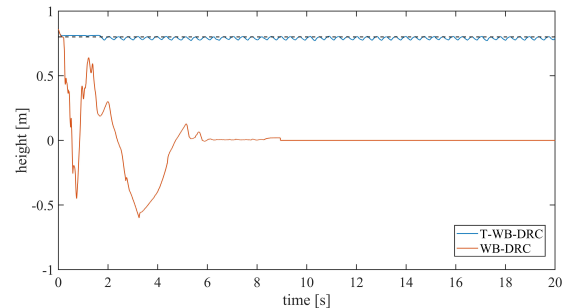


Fig. 12: The height of the humanoid robot's base link when the knee joint motor output torque is cut by 30% with $\omega_0 = 300$.

To demonstrate the ability to handle model uncertainties, we conduct a simulation comparison in which the humanoid robot holds an 8 kg load while trotting in place, as shown in Fig. 10. We select ESO as the disturbance estimator to estimate uncertainties and use the MAF as the signal processing module, with the moving horizon window as 7. Fig. 13 shows the base link height of the humanoid robot while holding an 8 kg load and trotting in place. It demonstrates that the robot using T-WB-DRC trots for the full 40 s, whereas the robot using standard WB-C falls after approximately 20 s.

VIII. EXPERIMENTAL VERIFICATION

In this section, we first conduct two comparison real-robot experiments on a single PC (Intel i7-13700KF, 3.4 GHz) with the quadruped A1 robot on flat ground, demonstrating the advantages of the proposed T-WB-DRC over WB-DRC

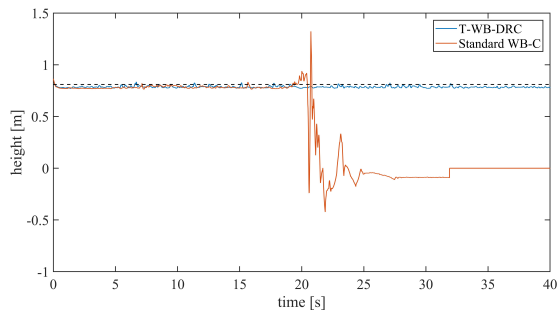


Fig. 13: The height of the humanoid robot's base link when the robot holds an 8 kg load.

and standard WB-C. We then perform a real-robot experiment on challenging terrain outdoor using a low-performance hardware platform, a microcomputer with an Intel i7-1165G7, 2.8 GHz. First, we reduce the knee joint output torque by 50% to evaluate the fault tolerance of the robot using three different methods. Next, the robot trots in place with a 5 kg load, as shown in Fig. 14, to assess its robustness to model uncertainties. Additionally, to demonstrate the control framework's ability to handle model uncertainties and external disturbances on rough terrain, we conduct experiments with the robot trotting on such terrain while carrying the 5 kg load, highlighting the T-WB-DRC's low dependence on hardware. The operating frequency for high-level control is set to 40 Hz with the prediction horizon $T = 1s$ and the total number of steps $H = 34$, while the low-level control operates at 1000 Hz with the prediction horizon $T_0 = 1s$ and the total number of steps $M = 34$. The robust MPC also operates at 40 Hz with the prediction horizon $T = 1s$ and discrete interval $\delta_t = 0.03s$. We choose MH-ESO as the disturbances estimator and the saturator as the signal processing module. The desired base link height is set to 0.31 m and the desired roll angles of the base link is set to 0 rad.



Fig. 14: The Unitree A1 robot with 5 kg load.

During the time intervals of 8.5s to 13.5s, 18.5s to 23.5s, 28.5s to 33.5s, and 38.5s to 43.5s, the output torque of one knee joint in each of the four legs is intentionally reduced by 50%, with a distinct knee joint subjected to torque reduction in each interval. Fig. 15 shows the height and roll angle of the robot's base link when the output torque of the four knee joints corresponding to the four legs is reduced by 50% for three different methods. As illustrated in Fig. 15, the robot employing T-WB-DRC demonstrates superior fault tolerance compared to both the robot using WB-DRC and the one utilizing standard WB-C. Fig. 16 illustrates the height and roll angles of the robot's base link while the robot trots in place, carrying a 5 kg load. As shown in Fig. 16, the height and

roll angles of the robot's base link using T-WB-DRC closely follow the desired trajectory, while the robot using the standard WB-C experiences a failure at nearly 10 seconds. These results indicate that T-WB-DRC demonstrates superior robustness to model uncertainties compared to both WB-DRC and standard WB-C.

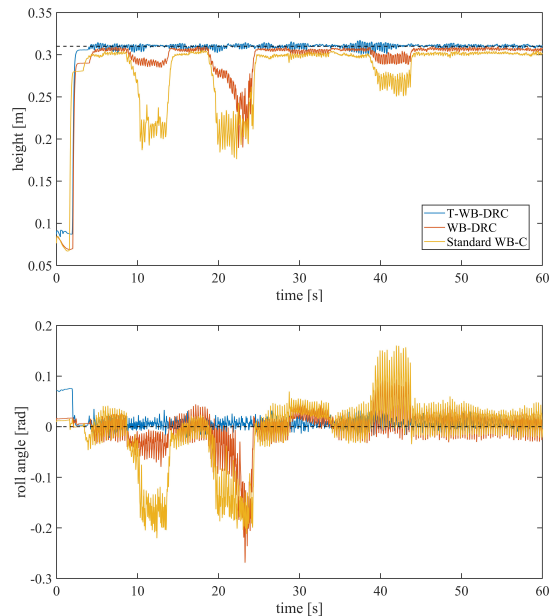


Fig. 15: The height and roll angle of the robot's base link when the output torque of the knee joints is reduced by 50%.

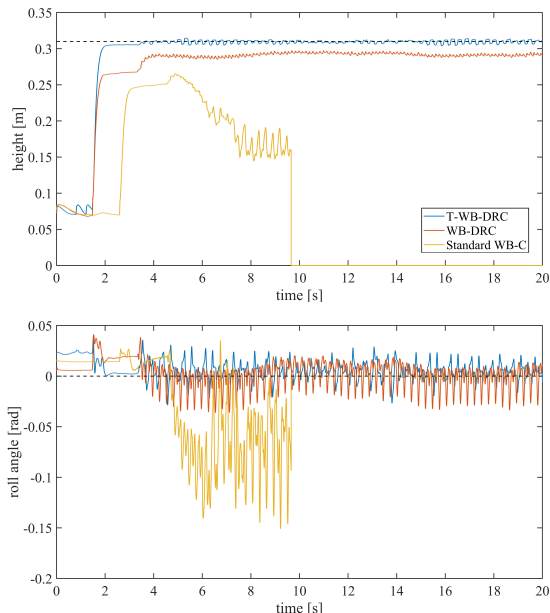


Fig. 16: The height and roll angle of the robot's base link while the robot trots in place with a 10 kg load.

To demonstrate the control framework's capability in handling model uncertainties and external disturbances on rough terrain, we conduct a real-robot experiment on challenging terrain. As shown in Fig. 17, the robot successfully navigates the rough terrain at a velocity of 0.2 m/s along the x -direction while carrying a 5 kg load, highlighting the effectiveness of the

proposed framework in enabling the robot to traverse difficult environments.

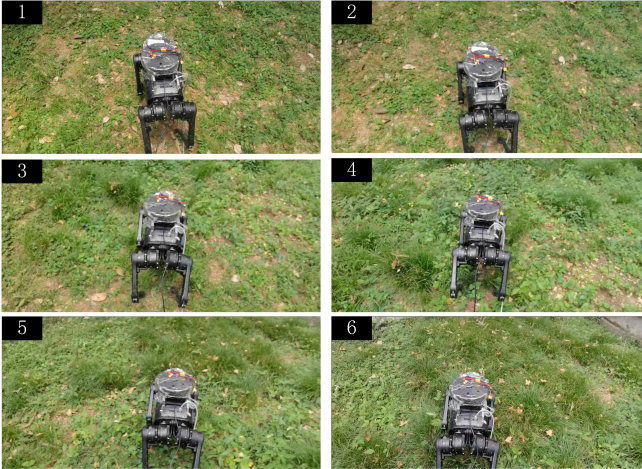


Fig. 17: The robot moves on tough terrain while carrying a 5 kg load.

IX. CONCLUSION

This paper presents an advanced control framework aimed at enhancing the stability and robustness of legged robots in the presence of various uncertainties, such as model uncertainties, external disturbances, and faults. The proposed framework integrates a MH-ESO to effectively estimate uncertainties and mitigate noise, ensuring accurate disturbance compensation. The introduction of the T-WB-DRC significantly improves robot performance by considering both uncertainty-free and uncertainty-affected dynamics, offering better payload transportation, disturbance rejection, and fault tolerance. Simulations on humanoid and quadruped robots demonstrate the framework's versatility, while experimental trials on a quadruped robot validate its robustness and stability under a wide range of disturbance conditions. Overall, the proposed T-WB-DRC offers a promising approach to improving the performance of legged robots in dynamic and unpredictable environments.

REFERENCES

- [1] D. Wisth, M. Camurri, and M. Fallon, "Vilens: Visual, inertial, lidar, and leg odometry for all-terrain legged robots," *IEEE Transactions on Robotics*, vol. 39, no. 1, pp. 309–326, 2022.
- [2] X. Meng, Z. Yu, X. Chen, Z. Huang, F. Meng, and Q. Huang, "Online adaptive motion generation for humanoid locomotion on non-flat terrain via template behavior extension," *IEEE Transactions on Automation Science and Engineering*, vol. 21, no. 4, pp. 6563–6574, 2023.
- [3] A. Luo, Q. Wan, Y. Meng, S. Kong, W. Chi, C. Zhang, S. Zhang, Y. Liu, Q. Zhu, and J. Yu, "Tfgait—stable and efficient adaptive gait planning with terrain recognition and froude number for quadruped robot," *IEEE Transactions on Automation Science and Engineering*, vol. 22, pp. 9218–9229, 2025.
- [4] Q. Li, Z. Yu, X. Chen, Q. Zhou, W. Zhang, L. Meng, and Q. Huang, "Contact force/torque control based on viscoelastic model for stable bipedal walking on indefinite uneven terrain," *IEEE Transactions on Automation Science and Engineering*, vol. 16, no. 4, pp. 1627–1639, 2019.
- [5] Y. Sun, W. L. Ubellacker, W.-L. Ma, X. Zhang, C. Wang, N. V. Csomay-Shanklin, M. Tomizuka, K. Sreenath, and A. D. Ames, "Online learning of unknown dynamics for model-based controllers in legged locomotion," *IEEE Robotics and Automation Letters*, vol. 6, no. 4, pp. 8442–8449, 2021.
- [6] B. Li, L. Zhu, and J. Huang, "Stable locomotion of biped robot with gaits of sinusoidal harmonics," *IEEE Transactions on Control Systems Technology*, vol. 32, no. 3, pp. 805–817, 2024.
- [7] M. Sombolostan and Q. Nguyen, "Adaptive force-based control of dynamic legged locomotion over uneven terrain," *IEEE Transactions on Robotics*, 2024.
- [8] S. Le Cleac'h, T. A. Howell, S. Yang, C.-Y. Lee, J. Zhang, A. Bishop, M. Schwager, and Z. Manchester, "Fast contact-implicit model predictive control," *IEEE Transactions on Robotics*, vol. 40, pp. 1617–1629, 2024.
- [9] S. Xu, L. Zhu, H.-T. Zhang, and C. P. Ho, "Robust convex model predictive control for quadruped locomotion under uncertainties," *IEEE Transactions on Robotics*, vol. 39, no. 6, pp. 4837–4854, 2023.
- [10] R. Grandia, F. Jenelten, S. Yang, F. Farshidian, and M. Hutter, "Perceptive locomotion through nonlinear model-predictive control," *IEEE Transactions on Robotics*, vol. 39, no. 5, pp. 3402–3421, 2023.
- [11] Z. Zhu, G. Zhang, Z. Sun, T. Chen, X. Rong, A. Xie, and Y. Li, "Proprioceptive-based whole-body disturbance rejection control for dynamic motions in legged robots," *IEEE Robotics and Automation Letters*, 2023.
- [12] G. Bledt, P. M. Wensing, S. Ingersoll, and S. Kim, "Contact model fusion for event-based locomotion in unstructured terrains," in *2018 IEEE International Conference on Robotics and Automation (ICRA)*. IEEE, 2018, pp. 4399–4406.
- [13] B. Li, W. Zhang, X. Huang, L. Zhu, and H. Ding, "A whole-body disturbance rejection control framework for dynamic motions in legged robots," *IEEE Robotics and Automation Letters*, pp. 1–8, 2025.
- [14] Z. Chen, Q. Xi, C. Qi, X. Chen, Y. Gao, and F. Gao, "Fault-tolerant gait design for quadruped robots with two locked legs using the gf set theory," *Mechanism and Machine Theory*, vol. 195, p. 105592, 2024.
- [15] Z. Luo, E. Xiao, and P. Lu, "Ft-net: Learning failure recovery and fault-tolerant locomotion for quadruped robots," *IEEE Robotics and Automation Letters*, vol. 8, no. 12, pp. 8414–8421, 2023.
- [16] H. Huang, W. He, J. Li, B. Xu, C. Yang, and W. Zhang, "Disturbance observer-based fault-tolerant control for robotic systems with guaranteed prescribed performance," *IEEE transactions on cybernetics*, vol. 52, no. 2, pp. 772–783, 2020.
- [17] X. Ren, J. Kou, Y. Cao, Q. Guo, Z. Chen, Y. Shi, and T. Li, "Fixed-time fault-tolerant control of robotic manipulators with actuator faults based on fixed-time extended state observer," in *2024 IEEE 63rd Conference on Decision and Control (CDC)*. IEEE, 2024, pp. 2074–2080.
- [18] H. Sun, R. Madonski, S. Li, Y. Zhang, and W. Xue, "Composite control design for systems with uncertainties and noise using combined extended state observer and kalman filter," *IEEE Transactions on Industrial Electronics*, vol. 69, no. 4, pp. 4119–4128, 2021.
- [19] A. A. Prasov and H. K. Khalil, "A nonlinear high-gain observer for systems with measurement noise in a feedback control framework," *IEEE Transactions on Automatic Control*, vol. 58, no. 3, pp. 569–580, 2012.
- [20] D. E. Orin, A. Goswami, and S.-H. Lee, "Centroidal dynamics of a humanoid robot," *Autonomous robots*, vol. 35, pp. 161–176, 2013.
- [21] D. E. Orin and A. Goswami, "Centroidal momentum matrix of a humanoid robot: Structure and properties," in *2008 IEEE/RSJ International Conference on Intelligent Robots and Systems*. IEEE, 2008, pp. 653–659.
- [22] G. Bledt, M. J. Powell, B. Katz, J. Di Carlo, P. M. Wensing, and S. Kim, "Mit cheetah 3: Design and control of a robust, dynamic quadruped robot," in *2018 IEEE/RSJ International Conference on Intelligent Robots and Systems (IROS)*. IEEE, 2018, pp. 2245–2252.
- [23] J. Di Carlo, P. M. Wensing, B. Katz, G. Bledt, and S. Kim, "Dynamic locomotion in the mit cheetah 3 through convex model-predictive control," in *2018 IEEE/RSJ international conference on intelligent robots and systems (IROS)*. IEEE, 2018, pp. 1–9.
- [24] M. Focchi, A. Del Prete, I. Havoutis, R. Featherstone, D. G. Caldwell, and C. Semini, "High-slope terrain locomotion for torque-controlled quadruped robots," *Autonomous Robots*, vol. 41, pp. 259–272, 2017.
- [25] Z. Gao et al., "Scaling and bandwidth-parameterization based controller tuning," in *Acc*, vol. 4, 2003, pp. 989–4.
- [26] M. A. Arteaga, "On the exact parameter estimation for robot manipulators without persistence of excitation," *IEEE Transactions on Automatic Control*, vol. 69, no. 1, pp. 410–417, 2024.
- [27] H. K. Khalil and J. W. Grizzle, *Nonlinear systems*. Prentice hall Upper Saddle River, NJ, 2002, vol. 3.
- [28] P. E. Gill, W. Murray, M. A. Saunders, and M. H. Wright, "Maintaining lu factors of a general sparse matrix," *Linear Algebra and its Applications*, vol. 88, pp. 239–270, 1987.
- [29] C. D. Bellicoso, C. Gehring, J. Hwangbo, P. Fankhauser, and M. Hutter, "Perception-less terrain adaptation through whole body control and hier-

archical optimization,” in 2016 IEEE-RAS 16th International Conference on Humanoid Robots (Humanoids). IEEE, 2016, pp. 558–564.